## FOCUS AREA SCIENCE TECHNOLOGY SUMMER FELLOWSHIP-2024

### Format for the final Report *,^

Name of the candidate : LAXMI PRASOON BARIK

Application Registration no. : FPHYS 39

Date of joining : 25.07.2024

Date of completion : 30.09.2024

Total no. of days worked : 68

Name of the guide : PROF. PRASHANT PATHAK

Guide's institution : INDIAN INSTITUTE OF TECHNOLOGY, KANPUR

Project title : ATMOSPHERIC CHARACTERIZATION USING SHACK-HARTMANN IMAGE MOTION MONITOR

**Address with pin code to which the certificate could be sent:**

POWERGRID BOYS HOSTEL, P.R.S.U., RAIPUR, C.G., 492010

E-mail ID: laxmiprasoon@gmail.com

Phone No: 9754580761

TA Form attached with final report : YES ✓ NO _____

If, NO, Please specify reason

_____
Signature of the candidate

Date: 01.10.2024

_____
Signature of the guide

Date: 01/10/24

**IMPORTANT NOTES:**
\* This format should be the first page of the report and should be stapled with the main report. The final report could be anywhere between 20 and 25 pages including tables, figures etc.
^ The final report must reach the Academy office within 10 days of completion. If delayed fellowship amount will not be disbursed.

Project Report

IASc-INSA-NASI FAST SUMMER FELLOWSHIP

# Atmospheric Characterization Using Shack-Hartmann Image Motion Monitor



Submitted by

**Laxmi Prasoon Barik**
Application No.: FPHYS39
Center for Basic Sciences, P.R.S.U. raipur, C.G.

Under the Supervision of

**Prof. Prashant Pathak**
Space, Planetary, Astronomical Sciences and Engineering
(SPASE)
Indian Institute of Technology, Kanpur

2024-25

# CERTIFICATE

This is to certify that the project entitled 'Atmospheric Characterization Using Shack-Hartmann Image Motion Monitor' is done by **Laxmi Prasoon Barik** under my guidance and supervision from 25th July 2024 to 30th September 2024 for the **IASc-INSA-NASI FAST SUMMER FELLOWSHIP 2024** for two months project at Space, Planetary, Astronomical Sciences and Engineering (SPASE), Indian Institute of Technology, Kanpur.

To the best of my knowledge and belief, this project embodies the work done by the candidate.

**Supervisor**

# ACKNOWLEDGEMENT

Laxmi Prasoon Barik

# Contents

# 1  Introduction

The roots of astronomy go back to ancient times. The night sky has always fascinated humankind. Mapping the sky has been a part of many cultures for navigation and other purposes. With current technological advancements, we can do much more. Observatories across the globe and sky enrich us with huge amounts of data. Telescopes have had remarkable success in the field of astronomy. We have ground-based and space-based telescopes across different wavelengths to study the night sky.

Astronomical imaging in ground-based telescopes requires various considerations such as selecting the observing site and building adequate infrastructures. Several key factors must be considered while choosing a location for observation: the site's accessibility, the climate, light pollution and atmospheric conditions. Space-based telescopes have a great advantage over ground-based telescopes in areas such as the absence of atmosphere and access to a wide range of wavelengths but they are costly and challenging to build.

Due to the dynamic variation in the Earth's atmosphere i.e. atmospheric turbulence, the resolving power of the ground-based telescopes is limited. This loss of resolution or blur due to turbulence is termed 'seeing'.

The wavefront arriving in the Earth's atmosphere can be considered a plane wavefront. Due to the turbulence, the wavefront is distorted. To get accurate images, these effects must be considered. The Full Width at Half Maximum (FWHM) of the point spread function (PSF) is a quantitative measure of seeing [5]. PSF is an image of a point source.

We can compare space-based and ground-based telescopes. Several advantages of a space-based telescope such as the Hubble space telescope and the James Webb space telescope are:

1. Absence of atmosphere

2. Access to a wide range of wavelengths

3. Continuous observation

However, they have limitations: High cost, limited lifespan, limited instrument upgrades, and maintenance.

Similarly, there are various advantages to building a ground-based observatory over a space-based observatory.

1. Lower cost and maintenance

2. Larger aperture sizes. Modern ground-based telescopes, such as the European Extremely Large Telescope (ELT), have mirrors far larger than any space-based telescope.

The limitations for ground-based observatories are: Atmospheric distortions, wavelength limitations, observation window constrained by Earth's rotation, and location dependence.

# 2 Turbulence Profiling

Optical turbulence occurs when layers of air of different temperatures resulting in different refractive index, mix. The atmospheric turbulence causes random speckling and movement of the image, called 'seeing', as well as intensity fluctuations, known as 'scintillation' [9].
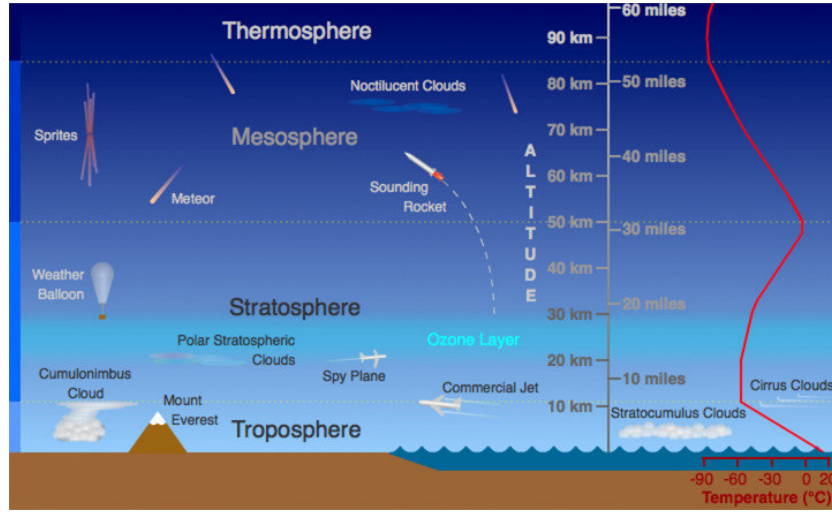


Figure 1: Typical atmospheric conditions in terms of altitude and temperature. Taken from Russell (2009).

The gradient of refractive index and dynamical turbulence caused by temperature and water vapor results in spatial and temporal fluctuations. They induce phase delays of different parts of the wavefront which deforms the plane wavefront.

## 2.1 Kolmogorov Model

Kolmogorov model is used to describe turbulence. It assumes that energy is inserted into a fluid medium on a large spatial scale, known as the outer scale $(L_0)$ and breaks down to form progressively smaller eddies. This continues until the turbulence energy is dissipated by the viscous properties of the medium at the inner scale $(l_0)$, i.e. where Reynolds number $R_e \approx 1$ [7].

It introduces the term 'structure-function', which describes the refractive index spatial fluctuations caused by atmospheric turbulence.

$$D_n(r) = \langle [n(\epsilon) - n(\epsilon + r)]^2 \rangle,$$

$$= C_n^2(h) r^{\frac{2}{3}}$$

Where n is the difference in refractive index, r is the separation, and $\epsilon$ is the position. The refractive index structure constant, $C_n^2(h)$, is a measure of the refractive index fluctuations. It is used to quantify the optical turbulence strength of layers at height, h.

The phase structure function can be described as:

$$D_\phi(r) = \langle [\phi(\epsilon) - \phi(\epsilon + r)]^2 \rangle,$$

The concept of the Fried parameter, isoplanatic angle and coherence timescale are also essential to account for. The Fried parameter $(r_0)$ is an important measurement for monitoring atmospheric optical turbulence, it is defined as the diameter of a circular aperture where the residual phase variance is 1 $rad^2$. The isoplanatic angle is the angular distance between two points on the sky over which the residual atmospheric wavefront phase variance is 1 $rad^2$. The coherence time is a measure of the timescale of the turbulence variation. As according to Hardy (1998), the phase structure function at the output of a thin layer with Kolmogorov turbulence is given by,

$$D_\phi(r) = 2.914 k^2 sec(Z) r^{\frac{5}{3}} \int_0^\infty C_n^2(h) dh$$

where Z is the zenith angle. For small spatial separation, Fried (1965)[6] simplified this to,

$$D_\phi(r << L_0) = 6.88 (\frac{|r|}{r_0})^{\frac{5}{3}},$$

where $r_0$ is the Fried parameter. It is a scale length that quantifies the integrated turbulence strength. It relates to $C_n^2(h)$ by

$$r_0 = (0.423 k^2 sec(Z) \int_0^\infty C_n^2(h) dh)^{-\frac{3}{5}}$$

where k is the wavenumber.

# 3 Seeing Monitors and Optical Turbulence Profilers

Several turbulence profilers and seeing monitors are currently being used across different observing sites in order to improve adaptive optics (AO) performance and optimizing telescope operation. Turbulence profilers measure and characterize the vertical distribution of the atmosphere whereas seeing monitors measure the overall effect of atmospheric turbulence.

## 3.1 Differential Image Motion Monitor (DIMM)

It is a seeing monitor, based on a small telescope. It is used to estimate the total integrated turbulence strength. It measures the differential motion for the images of the target star produced by the two subapertures within the telescope pupil. It employs a differential method. Its measurements are insensitive to tracking errors and telescope shake. However, the turbulence causes small differential motions [11]. The variance of the differential motion can be found using the centroid values of the two spots formed on the detectors.

The seeing angle of a long-exposure image can be computed from differential motion measurements on a star at zenith distance Z by,

$$\theta_{FWHM} = 0.98 \left(\frac{D}{\lambda}\right)^{\frac{1}{5}} \left(\frac{\sigma_\star^2 \cos(Z)}{K_\star}\right)^{\frac{3}{5}}$$

where $\sigma_\star$ is the variance in the differential motion, $\star$ represents either of the two directions of motion, longitudinal and transverse to the vector separation of the subapertures. K is a constant called the response coefficient and D is the subaperture diameter [9].

The variance can be calculated as;

$$\sigma^2 = \left\langle |c_1 - c_2|^2 \right\rangle - \left\langle |c_1 - c_2| \right\rangle^2$$

$$= \sigma^2{}_{c_1} + \sigma^2{}_{c_2} - 2cov(c_1 c_2)$$

where $c_1$ and $c_2$ are the centroid values [9].
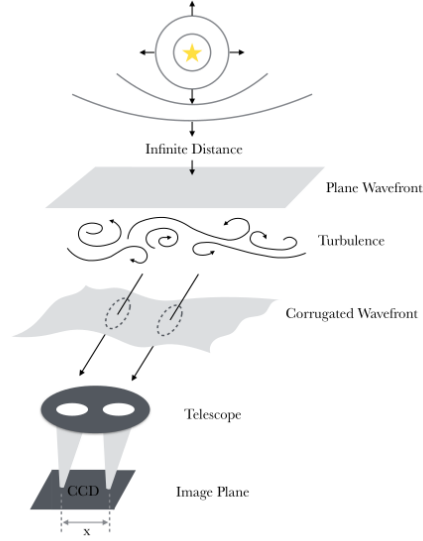
Figure 2:  Illustration of the classical DIMM. A CCD detects wavefronts distorted by the atmosphere via two subapertures focusing the light onto two spots separated by a distance x [9].

## 3.2   Multi Aperture Scintillation Sensor (MASS)

It is a turbulence profiler which measures the atmosphere in six layers. It does so by analyzing the spatial intensity fluctuations measured at the ground. The MASS instrument employs a four-ring aperture system to act as a spatial filter to establish scintillation originating from different altitudes. Each aperture is connected to a photomultiplier tube to detect the light of a single bright star [13].

Turbulence profiles can be represented as a collection of independent layers. The ten scintillation indices measured by MASS are modeled as

$$s^2{}_k = \int W_k(h) C^2{}_n(h) dh,$$

where $W_k(h)$ is the weighting function for the individual scintillation indices as a function of height, h [13].In order to understand the weighting functions, an understanding of the spectrum response and aperture geometry is required.

The atmosphere is modeled by MASS as a collection of six predefined heights, 0.5, 1, 2, 4, 8 and 16 km. It is not capable of sensing turbulence below
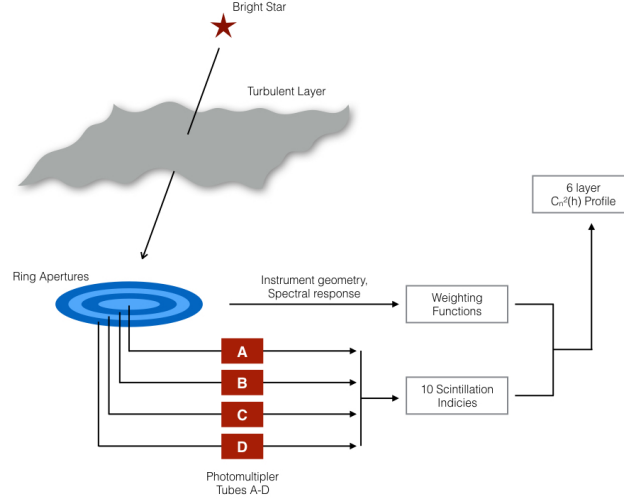
Figure 3: Illustration of the principles of MASS. Adapted from Tokovinin (2007) [13].

0.5 km. This is because it is difficult to differentiate weak scintillation in the presence of much stronger scintillation which originates at higher altitudes. [13]

## 3.3   SLOpe Detection and Ranging (SLODAR)

SLODAR is a vertical profiling technique that utilizes a Shack Hartmann Wavefront Sensor to image a pair of stars of known angular separation. The altitude, strength and velocity of each turbulent layer can be estimated using the triangulation method. The maximum altitude ($h_{max}$) and vertical resolution ($\delta h$) are determined by the geometry of the system as depicted in the figure. The value of $h_{max}$ is given by,

$$h_{max} = \frac{D}{\theta}$$

where D is the telescope aperture and $\theta$ is the angular separation of the target stars. The vertical resolution is given by,

$$\delta h = \frac{D}{n\theta} \times cos(Z)$$

Figure 4: Illustration of SLODAR geometry, where $\theta$ is the angular separation of the two target stars, $h_{max}$ is the maximum altitude, $\delta h$ is the altitude resolution and D is the diameter of the telescope aperture. Adapted from Osborn (2010) [8]

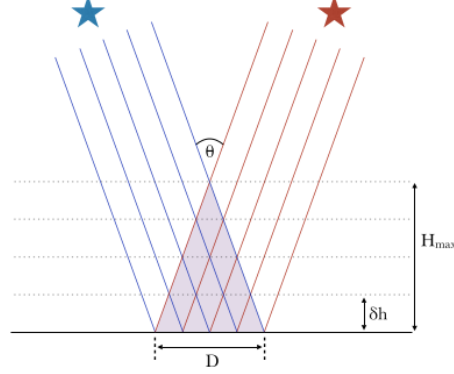where n is the number of subapertures subtended across the pupil and Z is the zenith angle of the observed target [8].

For each target star path, SLODAR estimates the spatial covariance of the gradient of the optical phase aberration observed at the ground [3]. By fitting the measured cross-covariance functions with a set of impulse response functions for the system, the turbulence profile can be recovered.

### 3.3.1 Obtaining Fried Parameter

The method used for estimating the Fried parameter ($r_0$) from SLODAR data is also used in Shack Hartmann Wavefront Image Motion Monitor (SHIMM). Firstly, the centroids of the spots, for individual frames are found using a standard center-of-mass algorithm. Telescope guiding errors and wind shake errors are removed by subtracting the mean of the centroids for each frame. Common tip and tilt motions induced by the atmosphere are also removed in this process. The response functions must be adjusted to take this into account.

A 2-D spatial cross-covariance map is produced from the centroids for the two target stars. A 1-D slice of the map is extracted, in the direction of the orientation of the stars on the focal plane [8]. The amplitude corresponds to

strength and position corresponds to the altitude of turbulent layers.

Precise estimations of $r_0$ for the entire atmosphere can be made by applying a fit to the auto-covariance of the centroids measured from the imaged spots for one wavefront sensor (WFS).

## 3.4   SCIntillation Detection And Ranging (SCIDAR)

SCIDAR also uses an optical triangulation technique similar to SLODAR. The turbulence profile is estimated from the correlation of the scintillation pattern produced by each star. For a turbulent layer at altitude h, two copies of the same wavefront aberration will be detected on the ground separated by a distance, $h\theta$, where $\theta$ is the angular separation of the two target stars. This results in a peak in the time-averaged spatial covariance of the image, at a separation corresponding to this distance. The amplitude of the correlation peak relates to the turbulence strength at h. From the temporal cross-covariance map, wind velocity can be found.
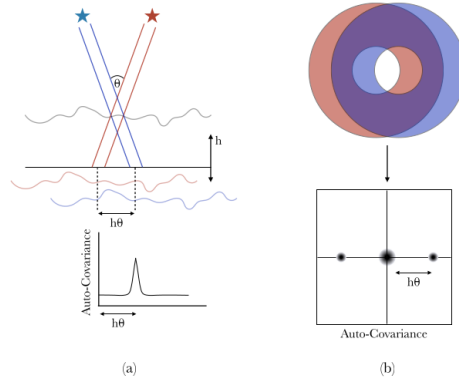


Figure 5: (a) Illustration of how two copies of the same wavefront aberration at altitude, h, will be detected on the ground at a distance $h\theta$, where $\theta$ is the angular separation. (b) The auto-covariance function generated from an overlapped pupil pattern image. Adapted from Shepherd et al.(2013) [12]

The theoretical vertical resolution for SCIDAR is dependent on the Fresnel radius size for a given altitude

$$\delta h(z) = 0.78 \frac{\sqrt{\lambda z}}{\theta},$$

where $z = |h - h_{conj}|$ and $h_{conj}$ is the conjugate altitude of the detector [10].

Variations on the SCIDAR have been made. One is LOLAS, based on a 40 cm telescope, designed for widely separated double star targets [1]. Another variation is the stereo-SCIDAR, which employs separate EMCCD detectors for each star, instead of a single detector [12].

# 4 Shack Hartmann Image Motion Monitor (SHIMM)

SHIMM is a low-cost, compact, portable seeing monitor. It can estimate coherence time ($\tau_0$) and low-resolution optical turbulence profile. Moreover, the effect of scintillation on $r_0$ can be corrected. It is a variation of the DIMM design, which employs a Shack Hartmann wavefront sensor instead of an aperture mask. SHIMM uses the SLODAR approach to estimate $r_0$ independent of noise, in contrast to DIMM, which measures seeing by relating the variance of the differential image motion obtained from pairs of subapertures to $r_0$.



Figure 6: The SHIMM (with additional FASS optics) at Cerro Paranal, Chile, at the site of the VLT [9].

### 4.0.1 Design and Working

SHIMM uses a lenslet array to map square subapertures onto the aperture of the telescope. Having as many subapertures as possible is preferable to make

full use of the telescope aperture. It also reduces statistical noise. However, large enough subapertures are required to provide a sufficient signal as well as a diffraction-limited spot width that is sufficiently small to permit the measurement of motions due to seeing. The spots must be Nyquist sampled meaning there must be at least 2 detected pixels across the FWHM of the spot.
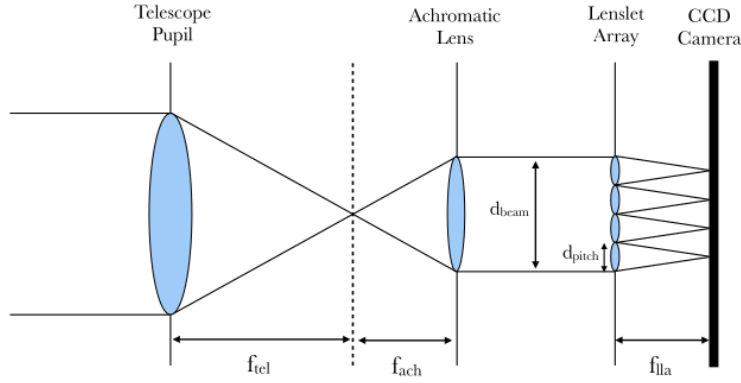


Figure 7: Schematic of the SHIMM optics. Light from the telescope is focused at $f_{telescope}$. The achromatic lens collimates the light into the lenslet array which focuses the light onto the CCD at $f_{lenslet}$ [9].

Several parameters are pre-defined: CCD pixel size $d_{pix}$, the telescope aperture $D$, f-number (N) and the desired number of subapertures n. f-number is the ratio of focal length to the telescope aperture.

($f_{lla}$) is the lenslet array focal length, ($f_{ach}$) is the collimating achromat focal length which is equal to:

$$f_{ach} = N \times d_{beam},$$

and $d_{beam}$ is given by

$$d_{beam} = n \times d_{pitch},$$

where $d_{pitch}$ is pitch width.

Given that there are limited combinations for $f_{ach}$, $f_{lla}$ and $d_{pitch}$, the combination is optimized to acquire the desired value of n and the largest sampling of the CCD.

# 5 Simulation

For simulation purposes, the PROPER optical propagation library is used. PROPER is a library of routines for Fourier-based wavefront propagation through an optical system. It was developed at the Jet Propulsion Laboratory for modeling stellar coronagraphs. It can also be used for simulating other optical systems where diffraction propagation is of concern.

In general, modeling the propagation of light through an optical system can be done in one of two ways: (1) Ray tracing, where the path of individual beams is calculated, or (2) Physical optics propagation(POP), where changes in the electromagnetic field are calculated as it travels. PROPER uses the latter. The PROPER routines implement common Fourier transform algorithms (angular spectrum and Fresnel approximation) to propagate a wavefront in near-field and far-field conditions. Depending on the characteristics of the pilot beam, the procedures automatically select the appropriate algorithm to use.

The effect of atmospheric turbulence must be considered during simulation. The propagation of the aberrated wavefront from the atmospheric phase screen to the ground is involved in the complex 2-D aberrated wavefront that is observed at the telescope pupil which is then passed to the simulated imaging system. The phase screen used in our system is generated using Von Kármán statistics. Von Kármán is an atmospheric turbulence profiling model that is more advanced than the Kolmogorov model with certain limits in the outer and inner scales. Figure 8(a) is a simple phase-screen generated using Von Kármán statistics. The phase change is given in radians. This means that to obtain the physical phase distortion in nanometres, it must be multiplied by $\lambda/(2\pi)$, where $\lambda$ is the wavelength in meters.

For simulation, the aperture size (D) is 11 inch. The number of subapertures is 6. Here the PSF is Nyquist sampled which can be seen in figure 9
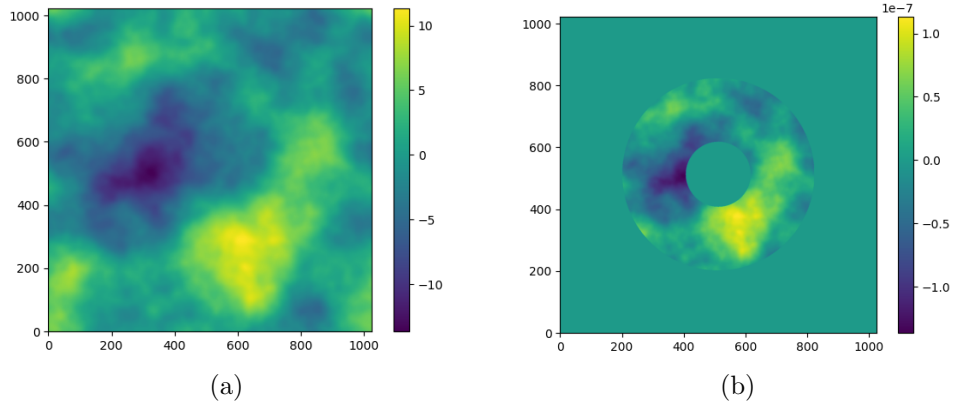
(a)

(b)

Figure 8: (a)A phase screen generated by using Von Kármán statistics with $r_0 = 0.15m$, outer scale $L_0 = 100m$ and inner scale $l_0 = 0.10m$, and (b)The pupil upon placing the phase screen (Note: The phase screen is scaled so that it matches the size of the pupil)
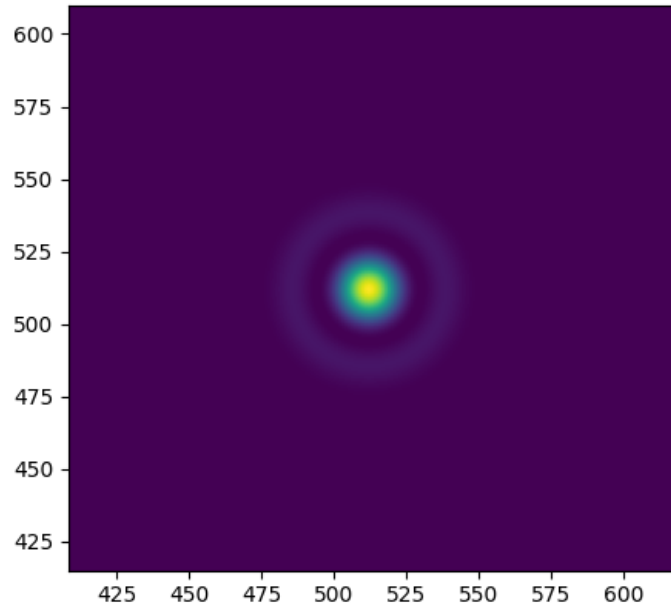


Figure 9: PSF after propagation through a lens.

## 5.1 Adding Noise

Image noise is a variation of brightness or color information in the image. Noise can originate from various sources. It is an undesirable part of the image. Noise is added to make the simulation more realistic. For our simulation, we are only considering read noise and photon noise.

### 5.1.1 Read Noise

Read noise is the amount of noise generated by electronics as the charge present in the pixels is transferred to the camera. It is almost always given in electrons.

In our simulation, read noise is generated using Gaussian distribution. The parameters which control the noise are: (1)The amount, which is magnitude of read noise in electrons, and (2) Gain, which converts this noise into analog-to-digital units (ADU).
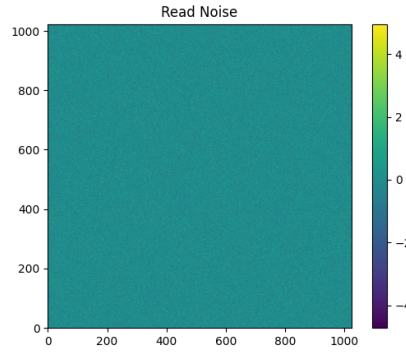


Figure 10: Read noise with amount=1 and gain = 1

### 5.1.2 Photon Noise

Photon noise or shot noise refers to the inherent natural variation of the incident photon flux. It is associated with statistical nature of electromagnetic waves. In other words, it is the randomness in the signal associated with photons which arrive at detector. It exhibit a Poisson distribution therefore it is known as Poisson noise. It is also called quantum noise. It has a square root relation with signal.

For simulation purpose a shot noise equal to square root of the original flux is added. The original flux is assumed to be 47600 photons/second for 1 second exposure time. This is calculated using the formula:

$$Flux = 10^{-0.4 \times \ apparent \ magnitude} \times Flux \ at \ magnitude(m = 0) \ (Jy)$$

$$1 Jy = 1.51 \times 10^7 \ photons/sec/m^2/(d\lambda/\lambda)$$

where $d\lambda/\lambda$ is the ratio of filter width $(d\lambda)$ to the central wavelength $(\lambda)$, taken to be 0.16 for V-band and flux at magnitude m $= 0$ is 3640 for apparent magnitude 10.



Figure 11: Poisson noise equal to square root of the original flux

The PSF after adding the noise is a more realistic case 12(b).
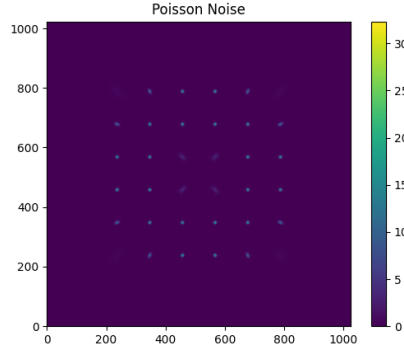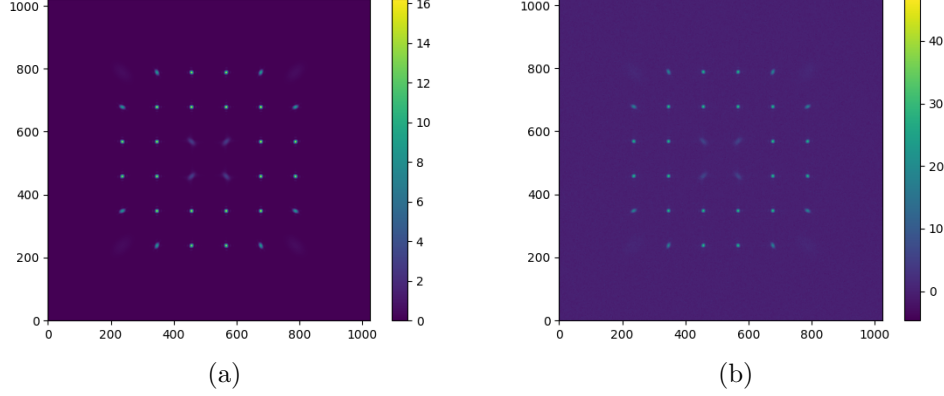
Figure 12: (a) psf after passing through the lenslet arrangement and (b) psf after adding noise

# 6   Spatial Covariance of the Slopes of the Phase Aberration

In order to estimate the profile of the turbulence strength, one needs to get spatial covariance of the slopes of the wavefront phase aberration at the ground. It is done for double star target by Butterley et al. (2006) [3].

They determine the impulse response for SLODAR as a function of the turbulence altitude, and also as a function of the spatial power spectral density of the phase fluctuations.

As discussed in section 3.3, the turbulence altitude profile is found via triangulation 4.

The 'impulse response' is the shape of the covariance for a thin layer at a given altitude. If the impulse responce of a system is known, then turbulence profile can be recovered via a fit to the measured cross-covarinace function.

The centroid data for the SHWFS are a measure of the slope of the wavefront over each subaperture [3].

$s_{i,j}^{x[1]}(t)$ is the slope in the x-direction for the subaperture [i, j] for the first star, where i and j index the position of a subaperture in the SH array horizontal (x) and vertical (y) directions at time t, for the first star. Similarly $s_{i,j}^{x[2]}(t)$ for the second star.

$$s_{i,j}^{x[1]} = \int \phi\left(w\boldsymbol{r}_{i,j}^{[1]}\right) F_x\left(\boldsymbol{r}_{i,j}^{[1]}\right) W\left(\boldsymbol{r}_{i,j}^{[1]}\right) \mathrm{d}\boldsymbol{r}_{i,j}^{[1]}$$

where $\boldsymbol{r}_{i,j}^{[1]}$ is a spatial coordinate, defined in units of subaperture width w, with its origin at the centre of subaperture [i,j] for star 1. $\phi\left(w\boldsymbol{r}_{i,j}^{[1]}\right)$ is the optical subaperture pupil function:

$$W(r) = 1 \;\; for|x|,|y| < 1/2$$
$$= 0 \;\; otherwise$$

,

and $F_x$ is the linear slope function in the relavant direction, normalized such that

$$\int F_x^2(\boldsymbol{r})W(\boldsymbol{r})\mathrm{d}\boldsymbol{r} = 1$$

The cross-covarinace of the slopes for the two subapertures is

$$C_{i,j,i',j'}^x = \left\langle s_{i,j}^{x[1]} s_{i',j'}^{x[2]} \right\rangle$$

for the slope in the x-direction between subapertures [i, j] for star 1 and $[i', j']$ for star 2.

The spatial offset between the subapertures in units of w is $(\delta i, \delta j) = (i' - i, j' - j)$. The angular brackets denote averaging over a large number of independent realizations of the turbulent distortions over the telescope.

The Longitudinal covariance for a pair of subapertures is given by

$$C_{i,j,i',j'}^x = \iint \left\langle \phi_{i,j}^{[1]}\left(w\boldsymbol{r}_{i,j}^{[1]}\right) \phi_{i'j'}^{[2]}\left(w\boldsymbol{r}_{i',j'}^{[1]}\right) \right\rangle F_x\left(\boldsymbol{r}_{i,j}^{[1]}\right) F_x\left(\boldsymbol{r}_{i',j'}^{[2]}\right)$$
$$\times W\left(\boldsymbol{r}_{i,j}^{[1]}\right) W\left(\boldsymbol{r}_{i',j'}^{[2]}\right) \mathrm{d}\boldsymbol{r}_{i,j}^{[1]}\mathrm{d}\boldsymbol{r}_{i',j'}\right)$$

The covariance of the slopes across two subapertures can be found via a numerical integral involving the spatial structure function, $D_\phi(wx)$,of the phase aberrations (Wilson and Jenkins 1996)

$$
\begin{aligned}
\left\langle \Phi_{i,j}^{[1]}\left(w\boldsymbol{r}_{i,j}^{[1]}\right) \Phi_{i',j'}^{[2]}\left(w\boldsymbol{r}_{i',j'}^{[2]}\right) \right\rangle &= -\frac{1}{2}D_\phi(w\boldsymbol{x}) \\
&+ \frac{1}{2}\int W\left(\boldsymbol{r}_{i,j}^{[1]}\right) D_\phi(w\boldsymbol{x})\mathrm{d}\boldsymbol{r}_{i,j}^{[1]} \\
&+ \frac{1}{2}\int W\left(\boldsymbol{r}_{i',j'}^{[2]}\right) D_\phi(w\boldsymbol{x})\mathrm{d}\boldsymbol{r}_{i',j'}^{[2]} \\
&- \frac{1}{2}\iint W\left(\boldsymbol{r}_{i,j}^{[1]}\right) W\left(\boldsymbol{r}_{i',j'}^{[2]}\right) D_\phi(w\boldsymbol{x})\mathrm{d}\boldsymbol{r}_{i,j}^{[1]}\mathrm{d}\boldsymbol{r}_{i',j'}^{[2]}
\end{aligned}
$$

where $\Phi_{i,j}^{[1]}\left(w\boldsymbol{r}_{i,j}^{[1]}\right)$ is the phase relative to the aperture mean,

$$
\boldsymbol{x} = \boldsymbol{u} + \boldsymbol{r}_{i',j'}^{[2]} - \boldsymbol{r}_{i',j'}^{[1]}
$$

and $\boldsymbol{u}$ is the vector separation of the subapertures in units of the subaperture width w, and is given by

$$
\boldsymbol{u} = (i' - i + \Delta, j' - j)
$$

where $(\Delta)$ is offset and equals $H\theta/w$

The shape of the slope covariance function depends on the underlying power law describing the spatial fluctuations of the phase. For the standard Kolmogorov model of atmospheric turbulence, the spatial spectrum of aberrations at the ground follows a power law with exponent -11/3.

Butterley et al. (2006) [3] have also explored the von Karman spectrum and the generalized spectrum .

The von Karman spectrum again assumes an underlying spectrum with slope -11/3, but the spectrum is modified to take into account the finite spatial outer scale of aberrations:

$$I_\phi(\kappa) = 0.022883 r_0^{-5/3} \frac{L_0^{11/3}}{(1 + L_0^2 \kappa^2)^{11/6}}$$

where $\kappa$ is the spatial frequency modulus, $r_0$ is the Fried parameter and $L_0$ is the outer scale. The corresponding form for the spatial structure function of the phase is (Jenkins 1998)

$$D_\phi(r) = 0.17253 \left(\frac{L_0}{r_0}\right)^{5/3} \times \left[1 - \frac{2\pi^{5/6}}{\Gamma(5/6)} \left(\frac{r}{L_0}\right)^{5/6} K_{5/6}\left(2\pi \frac{r}{L_0}\right)\right]$$

where K is a modified Bessel function of second kind.

For a given WFS and telescope pupil geometry, the individual subaperture tilt covariances (with global tilt correction) can calculated from equation of the longitudinal covariance for a pair of subapertures (6) via numerical integration.

## 6.1   SLODAR Response Function

For a turbulent layer at an altitude H, corresponding to an offset of $\Delta = H\theta/w$ in the x-direction (in units of w) between the projections of the telescope pupil on to the turbulent layer for the two stars, the covariance of the slopes for two subapertures after global tilt subtraction, is

$$C'^x_{i,j,i',j'}(\Delta) = \left\langle \left(s^{[1]}_{i,j} - \overline{s^{[1]}}\right)\left(s^{[2]}_{i'+\Delta,j'} - \overline{s^{[2]}}\right)\right\rangle$$
$$= \left\langle s^{[1]}_{i,j} s^{[2]}_{i'+\Delta,j'}\right\rangle - \left\langle s^{[1]}_{i,j} s^{[2]}\right\rangle - \left\langle \overline{s^{[1]}} s^{[2]}_{i'+\Delta,j'}\right\rangle + \left\langle \overline{s^{[1]}} s^{[2]}\right\rangle$$

where $\overline{s^{[1]}}$ is the slope for star 1 averaged over all subapertures, for example,

$$\overline{s^{[1]}} = \frac{1}{N_\text{sub}} \sum_{\text{valid } i,j} s^{[1]}_{i,j}$$

$$\left\langle \bar{s}^{[1]} S^{[2]}_{i'+\Delta,j'}\right\rangle = \frac{1}{N_\text{sub}} \sum_{\text{valid } i,j} \left\langle s^{[1]}_{i,j2} s^{[2]}_{i'+\Delta,j'}\right\rangle$$

where $N_{sub}$ is the total number of subapertures and valid i,j indicates all values of i and j for which the corresponding subaperture is not vignetted.

For SLODAR, Butterley et al. (2006)[3] averaged over all overlapping subapertures pairs for a given spatial separation $(\delta i, \delta j)$, taking into account teh projection of the telescope pupil function on to the subaperture array. The response of SLODAR to a turbulent layer at altitude H is therefore described by

$$X_{\mathrm{L}}(\Delta, \delta i, \delta j) = \frac{1}{N_{\mathrm{cross}}} \sum_{\mathrm{valid}\ i,j,i',j'} C'^{x}_{i,j,i',j'}(\Delta)$$

where $N_{cross}$ is the number of such existing subapertures where [i,j] and $[i', j']$ both exist.

The impulse response functions are two dimensional. However, two-dimensional information is only required if the velocities of the turbulent layers are to be measured. Velocity information can be obtained by introducing a temporal offset between the centroid data being correlated for the two stars and observing the resulting spatial offset of the peaks in the two-dimensional cross-covariance function. If only the turbulence strength as a function of altitude is required, all of the necessary information is contained in a cut through the two-dimensional covariance function in the x-direction, at y = 0. Hence, we can set j = $j'$ in previous equation to obtain a set of one dimensional response functions:

$$X_{\mathrm{L}}(\Delta, \delta i) = \frac{1}{N_{\mathrm{cross}}} \sum_{\mathrm{valid}\ i,j,i'} C'^{x}_{i,j,i',j}(\Delta)$$

The SLODAR impulse response functions are then found from the above equation by averaging over all overlapping subaperture pairs for each offset $\delta i$.

A measure of the vertical profile of atmospheric turbulence can now be found by fitting the altitude-dependent impulse response functions to the measured tilt covariance values.

# 7 Reconstruction

After passing through the atmosphere, the plane wavefront is distorted. This causes local chnages in the wavefront slope and corresponding changes in the directions of the rays. In order to reconstruct the wavefront, one must convert the array of slopes for each subaperture into the actual shape of the distorted front. This requires some integration-like algorithm, and the computations generally require a mathematical matrix inversion. For a large number of subaperture, this requires a very fast computer. Reconstruction is critical for guiding deformable mirrors to correct optical system and improve image quality.

The basic equation used by Shack-Hartmann testing is

$$\vec{\delta} = m f_{lla} \vec{\nabla} z$$

where $\vec{\delta}$ is the displacement of the subimages (in units of length), $m = f_{telescope}/f_{achromatic}$ is the demagnification of the system, $f_{lla}$ is the focal length of the lenslets, and z(x,y) is the aberration expressed in units of length. It is related to the phase aberration $\phi(x, y)$ as $\phi = kz$, where k is the wavenumber[4].

We also need the understanding of 'quad-cells' [13]. They are quadrant cells that are used to measure the position or centration of a focused spot of light. In [9], this is done by a standard centre-of-mass algorithm.

The x and y components of the subimage displacements can be approximated by:

$$\delta_x = \frac{b}{2} \frac{I_1 - I_2 - I_3 + I_4}{I_1 + I_2 + I_3 + I_4}$$

$$\delta_y = \frac{b}{2} \frac{I_1 + I_2 - I_3 - I_4}{I_1 + I_2 + I_3 + I_4}$$

where $I_j$ is the intensity at $j^{th}$ pixel nad b is the subimage diameter (in units of length). These expressions are true only in the limit that the displacements are small compared to b.
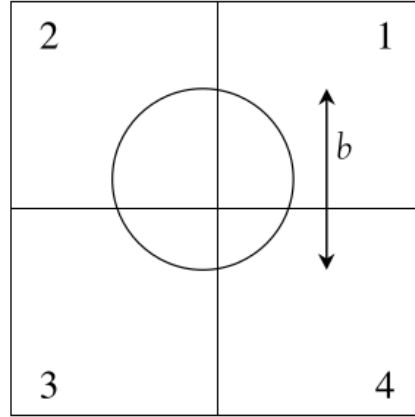
Figure 13: Arrangement of a quad cell. b is the subimage diameter in units of length [4]
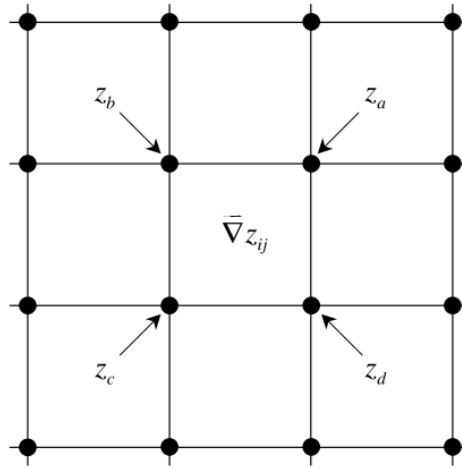


Figure 14: Representation of a portion of the (re-imaged) aperture plane in the square Shack-Hartmann geometry. Squares represent lenslets; filled circles represent phase points. [4]

In the quad cell implementation the overall system gain is imperfectly known as image diameter b is not directly measured.

We can get $\vec{\nabla}z$ but we need z.

Let the vertices between lenslets represent the 'phase points'. For a square array of $k \times k$ lenslets, there are $2k^2$ known gradient components.

A finite difference approach is suited. The gradient averaged over the lenlets may be approximated by:

$$\frac{\partial z}{\partial x} = \frac{1}{2\Delta}\left(z_a - z_b - z_c + z_d\right)$$

$$\frac{\partial z}{\partial y} = \frac{1}{2\Delta}\left(z_a + z_b - z_c - z_d\right)$$

where $\Delta$ is the lenslet side length mapped to primary mirror. The integration is thus reduced to a linear algebraic system of $m = 2k^2$ equations in $n = (k+1)^2$ unknowns.

This can be simply reduced to the following set of equations:

$$\mathbb{A}\vec{z} = \vec{b}$$

$$\mathbb{A} = \mathbb{U}\mathbb{W}\mathbb{V}^{\mathrm{T}}$$

$$\vec{z} = \mathbb{V}\mathbb{W}^{-1}\mathbb{U}^{\mathrm{T}}\vec{b}$$

where $\mathbb{A}$ is an $m \times n$ matrix defined by equations of gradient. $\vec{Z}$ is an n-dimensional column vector whose elements are the values of the aberrations at the phase points, and $\vec{b}$ is an m-dimensional column vector whose elements are the values of $\partial z/\partial x$ and $\partial z/\partial y$ corresponding to the lenslets.

$\mathbb{U}$ is an $m \times n$ column orthonormal matrix, $\mathbb{W}$ is an $n \times n$ diagonal matrix whose diagonal elements are all non-negative. $\mathbb{V}^{\mathrm{T}}$ is an $n \times n$ row and column orthonormal matrix [4].

# 8    Challenges and Future Prospects

SHIMM has a great advantage over traditional seeing monitors in many aspects including its accuracy in profiling and improved spatial resoltion in addition to its low-cost and portability.

SHIMM relies on sensitive detectors and precise image motion across a lenslet array.Thus, small calibration error can significantly affect the accuracy. It has limited performance in a situation of high turbulence. Integrating SHIMM with larger telescopes is quite complex.

As larger telescopes are developed, SHIMM can be adapted to provide real-time and high resolution data for them. In future, SHIMM can contribute in calibrating satellite optics by providing detailed data about Earth's atmosphere. If SHIMM can be integrated more directly with adaptive optics (AO) systems, it will provide more precise and real-time turbulence data to improve AO performance. This would enhance image quality in astronomy [2].

# 9    Conclusion

In the duration of the project, I was able to learn about the basic challenge faced by a ground based detector i.e. atmospheric turbulence. The procedure of observation can be divided into two parts: (1) Wavefront sensing, (2) Reconstruction of the wavefront. In order to do so, study about seeing and turbulence was done. PROPER Optical Propagation Library was used for simulation purpose. Generation of wavefront objects and propagating them through various apertures like circular aperture and rectangular aperture was done. Obscurations were also added for simulation purpose. PSF generation using simple systems were also simulated. I was able to generate random phase screen using Von Kármán statistics. To add the phase screen to the aperture we need to scale the phase screen and must ensure that during propagation Nyquist criteria must be fulfilled. PSF using Fourier transformation was also generated.

During the completion of the project, a python code was generated to simulate Shack Hartmann Image Motion Monitor with the aperture diameter of 11 inch, focal-ratio corresponding to f/10, and focal length of lenslet array

equal to 0.0142 meter. For number of subapertures equal to 6, the resultant psf can be seen in figure 12(a). Noise that must be compensated from the original image to get a better result were stduied. Simulation of read noise and photon noise to add them to the simulation to generate a more realistic scenario was done.

Study about various other seeing monitors and profilers, such as DIMM, MASS, SLODAR and SLIDAR which have many advantages and disadvantages over one another, was done.

SHIMM has a vast potential in modern observational astronomy. Its applications in turbulence profiling and coherence time estimation along with cost effectiveness and portability makes it distinguishable.

# References

[1] R. Avila, J. L. Avilés, R. W. Wilson, M. Chun, T. Butterley, and E. Carrasco. LOLAS: an optical turbulence profiler in the atmospheric boundary layer with extreme altitude resolution. *Monthly Notices of the Royal Astronomical Society*, 387(4):1511–1516, 07 2008.

[2] Jacques M. Beckers. Adaptive optics for astronomy: Principles, performance, and applications. *Annual Reviews 4139 El Camino Way, P.O. Box 10139, Palo Alto, CA 94303-0139, USA*.

[3] T. Butterley, R. W. Wilson, and M. Sarazin. Determination of the profile of atmospheric optical turbulence strength from SLODAR data. *Monthly Notices of the Royal Astronomical Society*, 369(2):835–845, 05 2006.

[4] Gary A. Chanan. Principles of wavefront sensing and reconstruction. 2004.

[5] Frederick R. Chromey. *To Measure the Sky*. Cambridge University Press, New York, 2010.

[6] D. L. Fried. Statistics of a geometric representation of wavefront distortion. *J. Opt. Soc. Am.*, 55(11):1427–1435, Nov 1965.

[7] John W. Hardy. *Adaptive optics for astronomical telescopes*. Oxford University Press, Oxford University Press, 1998.

[8] James Osborn, Richard Wilson, Timothy Butterley, Harry Shepherd, and Marc Sarazin. Profiling the surface layer of optical turbulence with SLODAR. *Monthly Notices of the Royal Astronomical Society*, 406(2):1405–1408, 07 2010.

[9] Saavidra Perera. *SHIMM: A Low-Cost Portable Seeing Monitor for Astronomical Observing Sites*. PhD thesis, Durham University, 2018.

[10] Jean-Louis Prieur, G. Daigne, and R. Avila. Scidar measurements at pic du midi. *Astronomy and Astrophysics*, 371(1):366–377, 2001.

[11] M. Sarazin and F. Roddier. The ESO differential image motion monitor. *A&A*, 227(1):294–300, January 1990.

[12] H. W. Shepherd, J. Osborn, R. W. Wilson, T. Butterley, R. Avila, V. S. Dhillon, and T. J. Morris. Stereo-SCIDAR: optical turbulence profiling with high sensitivity using a modified SCIDAR instrument. *Monthly Notices of the Royal Astronomical Society*, 437(4):3568–3577, 11 2013.

[13] A. Tokovinin and V. Kornilov. Accurate seeing measurements with MASS and DIMM. *Monthly Notices of the Royal Astronomical Society*, 381(3):1179–1189, 10 2007.